Additive Manufacturing 46 (2021) 102059

Contents lists available at ScienceDirect

Additive Manufacturing

journal homepage: www.elsevier.com/locate/addma

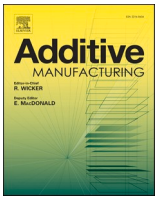

# Modular aerogel brick fabrication via 3D-printed molds

Piljae Joo [1], Yimin Yao [1], Nicholas Teo, Sadhan C. Jana [*]

*Department of Polymer Engineering, The University of Akron, Akron, OH 44325, United States*

ARTICLE INFO

*Keywords:*
Aerogels
Aerogel brick
3D mold
Additive manufacturing
Fused filament fabrication
Stereolithography

ABSTRACT

A 3D-printing process is presented for the manufacturing of modular aerogel/acrylate bricks that are fully scalable and customizable for potential applications in thermal insulation. The use of 3D-printing tools in conjunction with a sol-gel method of aerogel synthesis circumvents the geometric limitations of fabrication of large size load bearing aerogel articles. In this study, two-component aerogel bricks are manufactured from the low thermal conductivity of aerogels and 3D-printed load-bearing polymer bricks. For this purpose, aerogels are synthesized from polyimide and partially crosslinked stereolithography acrylate (SLA) resins. The aerogel materials are held by mechanically strong LEGO®-like bricks derived from fully crosslinked SLA resin and fully cured epoxy resin. The transient temperature profiles on brick surfaces due to contact heating and flexural and compressive properties of bricks filled with aerogel materials are discussed.

## 1. Introduction

Aerogels have gained tremendous attention in the research community since the discovery of the first silica aerogels in 1931 [1,2] motivated by an assortment of unique properties such as ultralow density, low thermal conductivity, and the power-law relationship between compressive modulus and bulk density. Aerogels are chosen as material candidates for catalyst support [3,4] and thermal insulation [5], nanoparticle filtration from the air [6–9], drug delivery [10] as demand for complex structures grow in architectural designs [11], automotive and aerospace industries [12]. Although silica aerogels were the first thermally insulating aerogel materials with low thermal conductivities of 15 mW/m-K with an approximate density of 150 kg $m^{-3}$ at room temperature in the air [13], their inherent brittle nature and sensitivity to moisture restrict silica aerogel applications under humid conditions and as structural parts that are curved or require bending capability. In this regard, polymeric aerogels are more robust and present the option of tailoring mechanical properties [14].

Two primary routes are followed in literature in fabricating polymeric aerogels - thermo-reversible gelation and the sol-gel process; examples of thermo-reversible gelation include polyether ether ketone [15,16] and syndiotactic polystyrene aerogels [17–20], while polyurea [21–23], polyurethane [24–26] and polyimide aerogels [14,27] are formed via sol-gel processes.

Amongst the different polymeric aerogels, polyimide aerogels find a strong interest in aerospace applications due to their excellent mechanical properties and superior chemical and thermal resistance. Meador et al. [14] successfully synthesized mechanically strong and flexible polyimide aerogels with tensile strengths of 4–9 MPa with thermal decomposition temperatures above 600 °C. Vivod et al. [28] reported the successful synthesis of optically translucent polyimide aerogels that exhibited 70% transmittance values, making them ideal as windowpanes for spaceships. Despite these advances, the limitations imposed by supercritical dryer size restrict the fabrication of complex-shaped, large size aerogel structures for thermal insulation. One potential workaround for such fabrication issues is to design modular, thermally insulating bricks that can be fabricated easily irrespective of the length scales, e.g., from a few millimeters to a few tens of centimeter, by invoking the 3D-printing capabilities in conjunction with one of the aerogel synthesis mechanisms. The 3D-printed solid polymer structures in the modular brick serve as the load-bearing element, while the aerogels parts provide thermal insulation. Such an approach was followed in this work.

Aerogel particles can be combined with binders to obtain the desired shapes of thermally insulating articles. Wernery et al. [29] formulated thermally insulating clay bricks by binding perlite aerogel fillers using an organic binder and observed reduction of thermal conductivity from 91 to 59 mW/(m-K) determined from the guarded hot plate method. While this brick approach potentially circumvents the size restrictions associated with the fabrication of aerogel structural forms, the

* Corresponding author.
*E-mail address:* janas@uakron.edu (S.C. Jana).
[1] These authors contributed equally to this work.

https://doi.org/10.1016/j.addma.2021.102059
Received 14 August 2020; Received in revised form 22 April 2021; Accepted 14 May 2021
Available online 2 June 2021

advantage of aerogels as lightweight materials cannot be fully realized due to much higher density binders and high binder to aerogel weight ratio. We show in this work that additive manufacturing tools can be invoked to alleviate the above concerns and to develop a manufacturing method that produces modular load-bearing thermally insulating bricks that can be easily put together to build a multitude of shapes and sizes. Recently, Teo et al. [30] demonstrated a method for the fabrication of arbitrary-shaped 3D polyimide aerogel structures using 3D-printing tools. These authors fabricated gyroid-shaped structures using a sacrificial mold made of high impact polystyrene. The mold was fabricated via a fused filament fabrication (FFF) process. This prior work served as a motivation for the present work.

Some research articles were published in the interim on 3D printing of complex shape aerogel articles, primarily based on direct ink writing (DIW) method [31–33]. In these cases, appropriate liquid ink viscosity was achieved either with high volume percent of the solid precursor materials or using low temperature. Zhao et al. [31] 3D-printed silica aerogel articles via DIW using a slurry of silica aerogel particles of 4–20 μm size in pentanol with at least 40 vol% particle loading. Jiang et al. [32] prepared cellulose ink at up to 6 wt% solid loading by dissolving cellulose filter paper in sodium hydroxide/urea solution and printed 3D structures via DIW method. Cheng et al. [33] also used DIW on cold plates to facilitate freezing of the solvents and reported 3D-printed Kevlar aerogel articles. It became apparent that not all aerogel systems can be 3D-printed into complicated shapes via DIW method as at times appropriate viscosity modifiers cannot be identified or the porosity and bulk density cannot be compromised, for example, by using high fraction of solids. This latter aspect is specifically true for thermal insulation applications as an increase of solid content in aerogel structures also reduces the overall porosity.

In this present work, a method was developed to circumvent the above issues for fabrication of modular polymeric aerogel bricks with LEGO®-like structures. The method combined 3D-printing of a photo-crosslinkable stereolithography (SLA) resin to obtain LEGO® blocks, 3D-printing of a sacrificial cage via FFF, and sol-gel transition of a low viscosity polyimide resin system in the open space of the LEGO blocks housed in the sacrificial cage, as schematically presented in Fig. 1. The hollow LEGO®-like bricks and sacrificial cages were 3D-printed respectively via SLA of an acrylate resin and via FFF process of high impact polystyrene. The LEGO®-shaped hollow bricks were designed with protruded perforated features, such as rhombus, circles, or squares distributed on the surfaces of the bricks. The perforated surface features served as channels for injection of precursor sol in the hollow bricks and for facilitating solvent exchange and supercritical drying of the gel after the sol-gel transition. The protruded surface features also enabled the joining of the individual bricks in a modular manner to form larger structures with the desired shape, overall length, and mechanical strength. We demonstrated the versatility of the new fabrication method by preparing five different types of LEGO®-like bricks of the following combinations: (1) polyimide aerogel/acrylate brick, (2) solid acrylate brick, (3) acrylate aerogel/acrylate brick, (4) epoxy/acrylate brick, and finally (5) polyimide aerogel/epoxy/acrylate brick. The method presented in this work offers an alternative for 3D-printing of complex shaped aerogel articles from an array of resin systems that are not amenable to DIW approach. We also believe that large thermally insulating and mechanical load bearing structures can be fabricated by assembling the composite LEGO® blocks. In this context, the method reported in this work is scale neutral if one looks beyond fabrication of the original SLA LEGO® blocks.

## 2. Experimental

The new fabrication method adopted in this work was used to prepare five different types of LEGO®-like bricks: (1) hollow acrylate brick with no-infill, (2) acrylate brick with cured epoxy in-fill, (3) acrylate brick with polyimide aerogel in-fill, (4) acrylate brick with 10% SLA aerogel in-fill, and finally (5) acrylate brick with an infill of polyimide aerogel particles embedded in epoxy. As is evident, type (1) bricks had only air in its holes, type (2) brick had all the holes filled with epoxy, and type (3)-(5) bricks had its holes filled with porous aerogel in-fills. In

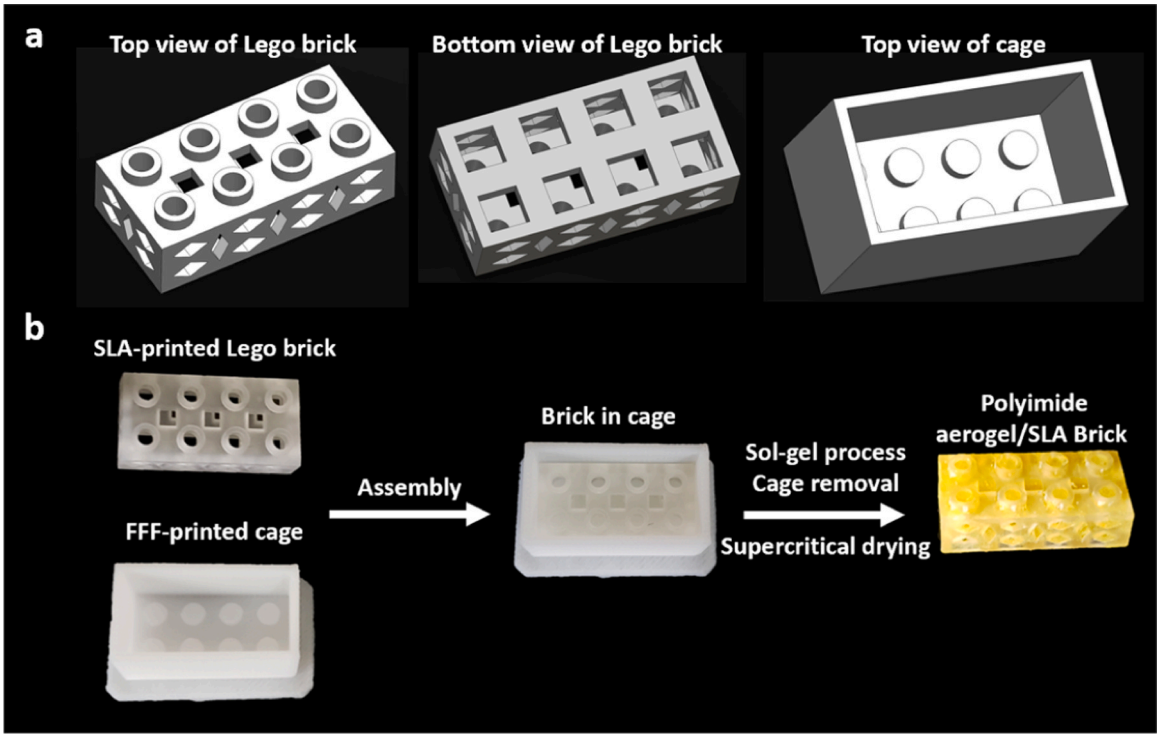


**Fig. 1.** (a) Design of brick and cage, (b) schematic illustration of the fabrication process of aerogel bricks from SLA hollow brick and FFF-printed cage and PI aerogel after supercritical drying.

conjunction, aerogel monoliths of polyimide and 10% SLA resin were fabricated. The materials and methods of fabrication of these materials are presented below.

## 3. Materials

Pyromellitic dianhydride (PMDA) was purchased from Alfa-Aesar (Haverhill, MA), 2,2′-dimethylbenzidine (DMBZ) was purchased from Shanghai Worldyang Chemical (Shanghai, China), and tris(2-aminoethyl)amine (TREN) crosslinker was obtained from Sigma Aldrich (Milwaukee, WI). Pyridine, acetic anhydride, and acetone were purchased from Fisher Scientific (Ontario, NY). N,N-dimethylformamide (DMF) and dimethyl sulfoxide (DMSO) were purchased from VWR International (Radnor, PA). Epon® 828 epoxy resin was obtained from Miller Stephenson (Danbury, CT), and Jeffamine® T403 curing agent was purchased from Huntsman (Houston, TX). A high-temperature SLA acrylate resin was purchased from Formlabs (Somerville, MA) and high impact polystyrene (HIPS) filament was purchased from MatterHacker (Foothill Ranch, CA).

## 4. Preparation of hollow LEGO® bricks

The LEGO® molds were designed in SOLIDWORKS® by replicating the dimensions provided on the LEGO® website, as shown in Fig. 1(a). The computer-aided design (CAD) model was modified to introduce perforated features on the brick surfaces. These perforated features acted as the reservoirs of precursor sol of aerogel and facilitated solvent exchange and supercritical drying process in subsequent steps. The hollow bricks were printed via SLA using a Form2 printer from Formlabs (Somerville, MA) starting with a high-temperature resin based on acrylates. Eighteen molds were printed each time over a time span of 5 hr. The printed molds were subjected to post-cure under UV exposure (405 nm) for 20 min to improve the mechanical and chemical resistance properties of the mold. The post-curing step was crucial to obtain resistance to solvents such as acetone, DMSO, and DMF used in the subsequent steps of aerogel synthesis and dissolution of the sacrificial cage. The sacrificial cages were printed from HIPS filaments using a Flashforge Creator Pro (Zhejiang, China) based on the FFF method. These cages housed the LEGO®-shaped hollow brick and served as the retaining container for the precursor sol; the sol infiltrated the hollow bricks (Fig. 1(a)) and subsequently underwent a sol-gel transition, all within the cage structure of HIPS. The cages were later dissolved in select solvents to recover the brick structure infiltrated with the gel.

## 5. Preparation of polyimide aerogel/acrylate bricks

The SLA-printed, post-cured acrylate bricks with its internal voids filled with polyimide aerogel were prepared as follows. The precursor sol was prepared at room temperature by dissolving PMDA and DMBZ separately in DMSO. These precursors were then mixed and magnetically stirred at 1000 rpm for 2 min to form polyamic acid oligomers. Subsequently, TREN, acetic anhydride, and pyridine were added to polyamic acid to obtain a crosslinked and chemically imidized three-dimensional network of polyimide gel. In a typical preparation, a polyimide sol with 6.7 wt% polymer concentration in DMSO was obtained through the addition of 0.42 g PMDA, 0.42 g DMBZ, 0.080 g TREN, 1.33 g acetic anhydride, 1.25 g pyridine, and 10.0 mL of DMSO. The polyimide sol was injected into the 3D-printed hollow bricks kept inside the supporting cage structure, as shown in Fig. 1(b). The sol-gel transition typically takes about 15 min at this polyimide concentration under a humidity-controlled laboratory environment of relative humidity of 50% at room temperature. The sol was left in the molds for at least 24 hr at room temperature to ensure complete crosslinking reactions [27]. The bricks filled with polyimide gel were subjected to solvent-exchange and simultaneous HIPS cage release by soaking in successive solvent mixtures of 100% DMF, 75% DMF / 25% acetone, 50% DMF/ 50% acetone, 25% DMF/ 75% acetone, and finally 100% acetone each at 12-hr intervals. In addition, the samples were washed with 100% acetone at least five times to ensure the removal of residual DMSO and DMF. The gels were then transferred into an autoclave, washed with liquid carbon dioxide, and dried under the supercritical condition of carbon dioxide at 50 °C and 11 MPa to obtain the polyimide aerogels. These materials are designated as “Polyimide aerogel/SLA”.

## 6. Preparation of solid acrylate bricks

These bricks were fabricated by injecting SLA resin into the hollow SLA brick kept inside the HIPS cage and curing the resin by exposure to UV radiation (405 nm) for 20 min. The cage was subsequently dissolved to obtain the 100% SLA resin bricks, which were dried under ambient conditions. Such materials are designated as “100% SLA/SLA” in the rest of the paper.

## 7. Preparation of acrylate aerogel/acrylate bricks

These bricks were fabricated in a similar process to the solid acrylate bricks presented above. The SLA resin was diluted in DMSO to 10 wt% concentration prior to injection into the SLA hollow brick kept inside the HIPS cage. This SLA resin was cured using 405 nm UV light for 20 min to obtain a crosslinked gel network of SLA with the pores filled with DMSO. Subsequently, the SLA gel was subjected to solvent exchange and supercritical drying steps as in the case of polyimide aerogel fabrication presented earlier. A porous acrylate aerogel structure contained inside the SLA brick was obtained. These materials are labeled as “10% SLA/SLA” in the rest of the paper.

## 8. Preparation of epoxy/acrylate bricks

Epon® 828 epoxy resin and Jeffamine® T403 curing agent were mixed at 7:3 ratio at 2500 rpm for 2 min in DAC 150.1 FVZ-K SpeedMixer (FlackTek Inc., SC). The epoxy and curing agent mixture was injected into the hollow SLA brick kept inside the sacrificial HIPS cage and cured at 80 °C overnight. The epoxy bricks, designated as “Epoxy/SLA” were recovered by dissolving the HIPS cage in DMF and drying under ambient conditions.

## 9. Preparation of polyimide aerogel/epoxy/acrylate bricks

Monolithic cylindrical polyimide aerogels were first fabricated in syringe molds by conducting sol-gel transition, solvent exchange, and supercritical drying [27]. The monolith was crushed to form polyimide aerogel particles of approximately 1 mm in size. These polyimide aerogel particles were mixed with the epoxy/curing agent mixture in 1:19 wt ratio and injected into the SLA hollow brick kept inside the HIPS cage. The epoxy to amine curing agent weight ratio was 7:3. The epoxy was cured at 80 °C overnight and the cage was subsequently dissolved to obtain the epoxy/polyimide/SLA bricks. Such materials are designated as “Polyimide aerogel/epoxy/SLA”. The weight ratio of polyimide and epoxy and the bulk and skeletal density of respectively polyimide aerogel and cured epoxy were used in calculation of volume fraction of polyimide aerogel granules in the infill material of the brick.

## 10. Preparation of monolithic polyimide aerogel, epoxy, epoxy/polyimide aerogel, 100% SLA resin and 10% SLA resin for thermal conductivity measurements

Monolithic cylindrical polyimide gel, cured epoxy in HIPS cage, cured epoxy-containing polyimide aerogel particles of ~1 mm size in HIPS cage, post-cured 100% SLA resin in HIPS cage, and acrylate gel synthesized from 10% SLA resin in HIPS cage were prepared separately following preparation methods used earlier for the brick materials. The cages were dissolved in DMF. The polyimide gel and acrylate gel from

10% SLA resin were subjected to solvent exchange in acetone and supercritical drying in liquid carbon dioxide for 12 hr. The 10% SLA gel was also allowed to dry in ambient air at room temperature for 24 hr. Other specimens were washed in acetone and air-dried.

## 11. Characterization

The original premise of fabricating acrylate bricks with aerogel in-fill was to draw from the load bearing capability of the acrylate bricks and the low thermal conductivity of low-density aerogels. In view of this, some of the properties, such as density, porosity, BET surface area, and stress-strain diagrams of aerogel specimens were separately evaluated. The thermal conductivity of aerogel materials is widely reported in literature. As will be apparent, the bricks with aerogel-infill were not uniform in spatial composition of the SLA and aerogel parts. Thus, thermal conductivity measurements with techniques such as laser flash method would yield distribution of thermal conductivity values on measurement plane. In view of this, we resorted to thermal imaging of the brick assemblies. This allowed us to infer the contributions of thermal insulation of the aerogel parts in the brick.

## 12. Flexural bending test

The force vs. displacement curves of the bricks were measured using an Instron 5966 Materials Testing System (Norwood, MA) with an apparatus for three-point bending tests. A 2580–10 kN high-resolution load cell was used with a displacement rate of 1.3 mm/min.

## 13. Stress vs. strain behavior

The stress vs. strain behavior of the samples was obtained using an Instron 5567 tensometer (Norwood, MA). A 1 kN load cell was used with a compression rate of 1.3 mm/min following the ASTM D695–15 method, which is equivalent to ISO 604.2.

## 14. Porosity and pore volume

Porosity was calculated from the values of skeletal ($\rho_s$) and bulk density ($\rho_b$) as shown in Eq. (1). The values of skeletal density were obtained using a helium pycnometer (AccuPyc II 1340, Micromeritics Instrument Corp., Norcross, GA). Bulk density was obtained from the mass and volume of aerogel specimens.

$$porosity = \left(1 - \frac{\rho_b}{\rho_s}\right) \times 100\% \quad (1)$$

## 15. Brunauer-Emmett-Teller (BET) surface area

BET surface area of aerogel specimens was obtained from $N_2$ adsorption-desorption isotherms at 77 K using a Micromeritics Tristar II 3020 analyzer (Micromeritics Instrument Corp., Norcross, GA).

## 16. Morphology

The morphology of aerogels was studied using a scanning electron microscope (SEM, JSM5310, JEOL, MA) at an accelerating voltage of 5 kV and an emission current of 20 mA. A representative piece of fractured aerogel specimen was mounted on an aluminum stub using carbon tape, followed by sputter coating with silver (ISI-5400 Sputter Coater, Polaron, UK).

## 17. Thermogravimetric analysis (TGA)

TGA was conducted under $N_2$ with a Q50 thermogravimetric analyzer (TA Instruments, Waltham, MA) using a heating rate of 10 °C/min, up to 650 °C.

## 18. Thermal conductivity and thermal imaging

The thermal conductivity was measured on a modified transient plane source followed by ASTM D7984 – 16 method at 21 °C using a TCI Thermal Conductivity Analyzer (C-Therm Technologies, New Brunswick, Canada). The thermal images were captured using a Fotric 225 IR camera (FOTRIC Thermal Imaging Technology Company, Dallas, TX). For this purpose, the aerogel bricks were placed on the FFF printer bed and the temperature of the bed was set at 120 °C. The images were taken once the bed temperature was stabilized at the set temperature.

## 19. Results and discussion

The optical images of various bricks fabricated following the methods presented in this work are shown in Fig. 2. It was observed that the in-fill of the bricks did not experience significant change in size or shape. The supercritical drying also kept shrinkage of the in-fill polyimide and 10% SLA resin aerogel part to a minimum.

The brick materials containing polyimide aerogel appeared with a characteristic amber color of polyimide. The acrylate aerogel obtained from a 10 wt% solution of SLA resin in DMSO appeared opaque. The polyimide aerogel/epoxy/SLA brick show amber color (Fig. 2) due to the presence of 5 wt% polyimide aerogel granules embedded in transparent cured epoxy. The skeletal and bulk density data reported in Table 1 indicate that the infill of the bricks of polyimide aerogel/epoxy/SLA contained ~80 vol% polyimide aerogel granules (bulk density 0.01482 g/cm$^3$) embedded in cured dense epoxy (skeletal density 1.1428 g/cm$^3$).

The importance of the post-curing step of SLA bricks is illustrated using the images presented in Fig. 3. The first set of images listed under "Without post-curing" were obtained by dipping the bricks in different sets of solvents – acetone, DMSO, and DMF for 24 hr. These images revealed that the bricks experienced swelling when immersed in the solvents and shrinkage and crack formation upon drying. In contrast, no significant deformation or damage was observed for the post-cured bricks. In view of this, post-cured SLA acrylate resin bricks were used as the skeletal framework in all composite brick structures.

In the first part of this work, monolithic cylindrical aerogels were fabricated from both polyimide and 10 wt% solutions of acrylate resin to assess their characteristics before developing the composite brick materials with post-cured SLA hollow bricks as shown in Fig. 1(a) and Fig. 2. The SLA acrylate resin gels were synthesized by UV curing of 10 wt% solution of the resin in DMSO. The solvent DMSO was removed from the gel by two different methods, namely through ambient air drying and supercritical drying. The optical images in Fig. 4 show that air-drying led to significant shrinkage of the aerogel specimens due to the capillary forces of the evaporating solvent from the small pore structure of the gel [34]. In contrast, the supercritically dried specimen nearly retained the shape and size of the gel specimen. The actual sizes of specimens produced by supercritical and air-drying are shown in Table S1 in Supplementary Information.

The BET data and SEM images presented in Fig. 5 indicate the successful preparation of porous polyimide and SLA resin aerogels aided by supercritical drying. However, the specific surface area of polyimide aerogel ~478 m$^2$/g was more than ten times compared to SLA resin aerogels, ~34 m$^2$/g. The hysteresis in adsorption-desorption isotherms in Fig. 5(a) also indicates significant mesopores in polyimide aerogels as noted by other researchers [14,27]. The SLA aerogel, however, did not show a hysteresis loop in Fig. 5(a) and therefore did not have much mesopore fractions. The morphologies of both aerogels are shown in SEM images in Fig. 5(b) and **5(c)**. It is apparent that polyimide aerogels were composed of strand-like polymer domains while the primary structure of SLA resin aerogel was composed of fractal-type aggregates of spherical polymer domains as was earlier observed in the cases of acrylate aerogels [35]. The polyimide aerogel part in polyimide/epoxy/SLA bricks were embedded in cured dense epoxy and were

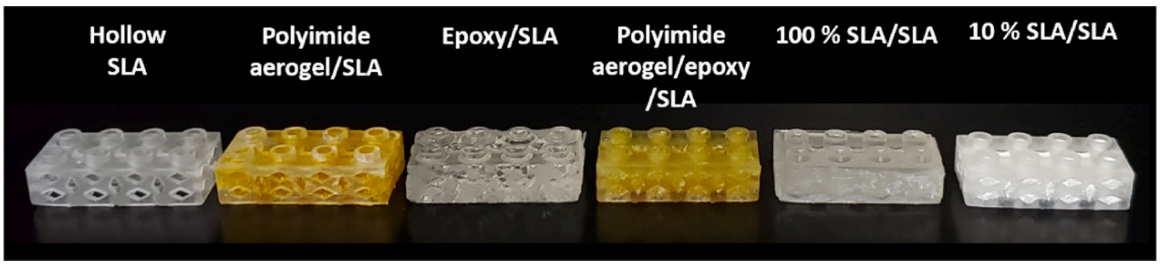


**Fig. 2.** Hollow SLA brick and bricks filled with various cured resins and aerogels.

**Table 1**
Bulk density, skeletal density, and porosity of aerogel monoliths and other materials.

| Material | Bulk density (g/cm$^3$) | Skeletal density (g/cm$^3$) | Porosity (%) |
|---|---|---|---|
| Polyimide aerogel monolith | 0.01482 | 1.3973 | 98.9 |
| 10% SLA aerogel monolith | 0.1397 | 1.2191 | 88.5 |
| 100% SLA monolith | 1.1444 | 1.2135 | 5.7 |
| Polyimide aerogel/epoxy monolith | 0.9074 | 1.1245 | 19.3 |
| Epoxy monolith | 1.0776 | 1.1428 | 5.7 |

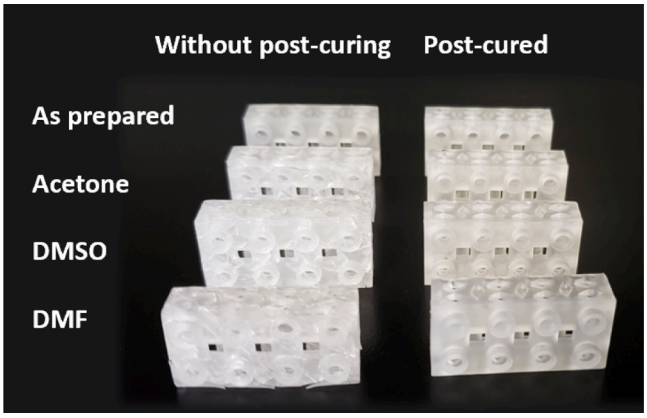


**Fig. 3.** Images of bricks with and without post-curing after immersion in acetone, DMSO, or DMF solvents for 24 h.

not accessible for surface area measurement via nitrogen adsorption-desorption experiments.

Next, we compared the mechanical properties of supercritically-dried polyimide and SLA resin aerogel in monolithic form. The compressive stress vs. strain curves of these two aerogel specimens is shown in Fig. 6. The compressive stress vs. strain curve can be categorized into three different regions. In the case of polyimide aerogel, the first region involves the deformation of the primary skeletal structure of the aerogel with the load borne by the skeletal struts of the porous structure. The second region involves a plateau region attributed to the collapse of the skeletal structure and compression of the pore volume. In the third and final region, the stress increased drastically with applied strain as if for a solid polyimide polymer with all its pores removed. The final region is apparent for polyimide aerogel sample at strain values of 0.6 mm/mm or higher. In the case of SLA resin aerogel, the plateau region was not apparent and the final region of stress vs. strain behavior was prominent from a strain of 0.4 mm/mm and higher. This compressive stress-strain behavior is consistent with other porous materials, as observed by Swyngedau [36].

The difference in mechanical properties between polyimide and SLA resin aerogel samples originate from the monomers used in each case. The polyimide samples utilized predominantly aromatic monomers, adding strength and stability to the synthesized crosslinked polymer structure, while the acrylate resin used linear aliphatic chains. Another factor is the difference in crosslink density. The images presented in Fig. 6(b) indicate that the polyimide aerogel sample retained its monolithic cylindrical shape during the compression test, while the acrylate aerogel exhibited brittle fracture.

The modular LEGO®-like polyimide aerogel/SLA bricks can be put together in any structural form on a base plate; a representative image is shown in Fig. 7(a). It is apparent that the polyimide aerogel/SLA bricks can be connected and stacked, just like the traditional LEGO® blocks. Three- and four-block configurations of SLA bricks are shown in Fig. 7(c) and (d) respectively, while a four-block arrangement of polyimide aerogel/SLA bricks is shown in Fig. 7(e). These structures were subjected to a flexural bending test (Fig. 7(c–e)), with the corresponding force vs. displacement curve shown in Fig. 7(b).

The force vs. displacement curve shows that the inclusion of polyimide aerogel did not improve the mechanical properties of the 4-block configuration in comparison to the flexural bending result of a corresponding 4-block configuration of hollow SLA bricks without the polyimide aerogels (Fig. 7(b)]). The 4-block SLA brick withstood a force of 157 N and flexural displacement of 1.2 mm compared to a force of 110 N and flexural displacement of 0.8 mm with Polyimide aerogel/SLA brick specimen. Interestingly, both the 4-block configurations using different materials exhibited the same flexural modulus, as gleaned from the slope of the curves shown in Fig. 7(b). This was because SLA bricks played a more important role in mechanical properties than polyimide aerogel and the fracture strength was dependent on minor defects introduced in printed bricks. The states of failure in these specimens are shown in Fig. 7(f) and (g). We contend that the polyimide aerogel did not contribute to the mechanical properties of the composites. In this context, one may question if there was good adhesion between SLA block and polyimide aerogel and if such adhesion played any role on shrinkage of supercritically dried aerogel in-fill. The images presented in Fig. S1 (Supplementary Information) indicate good adhesion between SLA domain and aerogel materials. However, quantification of such adhesion on shrinkage reduction of aerogel in-fills was beyond the scope of this work. The effects of solvent exchange and supercritical drying on the shape of SLA bricks and their mechanical properties were evaluated. The optical images in Fig. S2(a) establish virtually no change of shape of the SLA brick. The compressive load vs. displacement diagram in Fig. S2 (b) shows that up to 0.6 mm of displacement, the load of as prepared SLA bricks was close to that of SLA bricks subjected to supercritical drying.

The mechanical properties data of polyimide aerogel/epoxy/SLA brick are not reported here. In this case, the infill material was formed by dense epoxy phase with embedded granules of polyimide aerogel. These bricks supported an order of magnitude higher load than the open, porous infill of polyimide aerogel and about a factor of two higher load than the SLA brick as reported in Fig. S2(b).

We now discuss the bulk and skeletal density values and the overall porosity of the aerogel monoliths (polyimide and 10% SLA aerogel) and post-cured 100% SLA resin, cured epoxy, and polyimide aerogel /cured

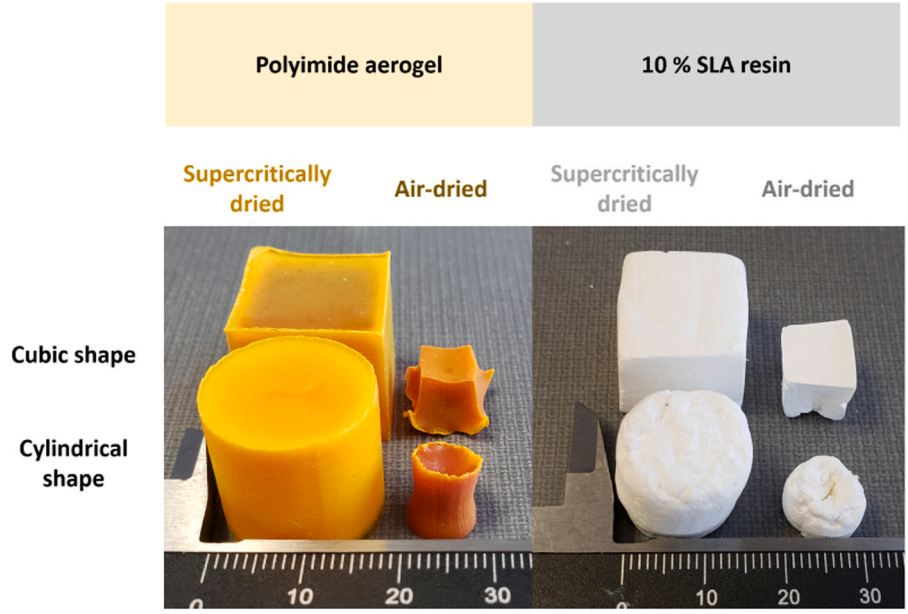


**Fig. 4.** Relative size of aerogel specimens obtained by supercritical drying and air-drying of polyimide gel and 10%SLA resin gel. The cube dimension was 20 mm × 20 mm × 20 mm and the diameter and height of the cylindrical specimen were 20 mm and 20 mm respectively.

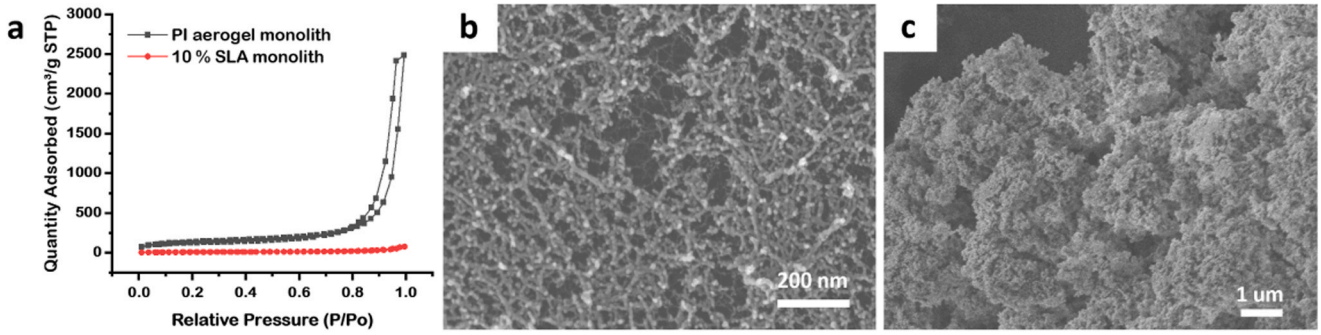


**Fig. 5.** (a) BET isotherms of PI and 10% SLA resin aerogel. (b) SEM image of PI aerogel and (c) 10% SLA resin aerogel.

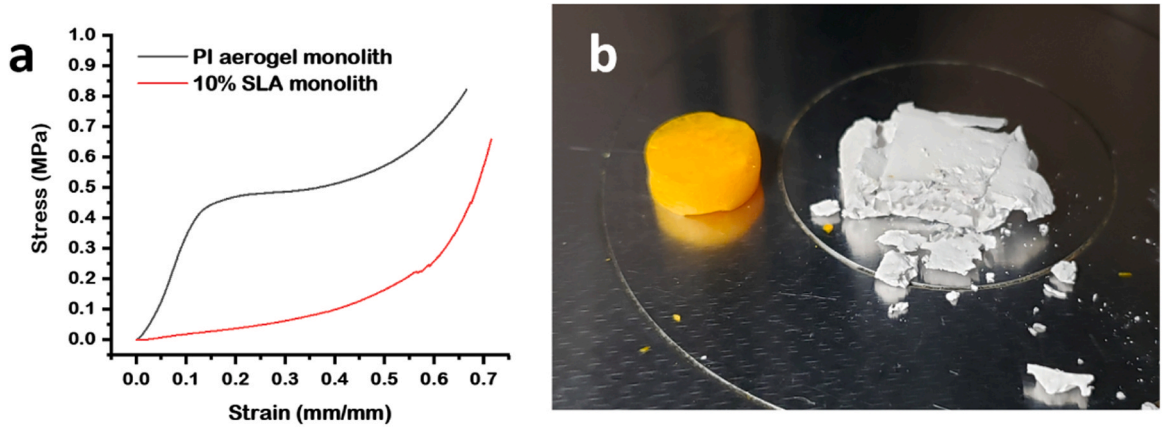


**Fig. 6.** (a) Compressive stress vs. strain curves of monolithic cylindrical polyimide and 10 wt% SLA resin aerogel specimens. (b) Optical images of samples after the compression test – amber yellow is PI and white is SLA. (For interpretation of the references to colour in this figure legend, the reader is referred to the web version of this article.)

epoxy mixture. The brick specimens were not used in this case to decouple the contribution of post-cured 100% SLA resins. Table 1 lists the values of bulk density, skeletal density, and porosity.

The data in Table 1 show that only the polyimide and 10% SLA aerogel monoliths exhibited high porosity of 98.9% and 88.5% respectively. This can be attributed to their porous nature seen in Fig. 5(b) and (c). These monoliths also show low bulk densities of 0.014 and 0.140 g/cm$^3$ respectively. The skeletal density values of these materials varied in

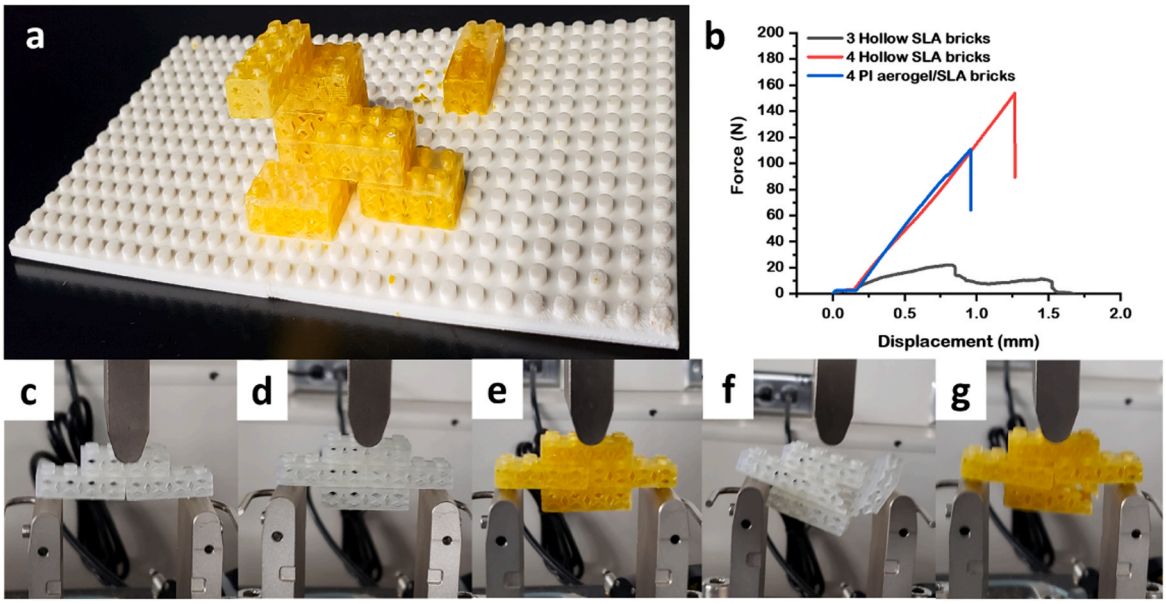


**Fig. 7.** (a) Assembled polyimide aerogel/SLA bricks, (b) Force vs. displacement curves in flexure test of specimens (c) 3 hollow SLA bricks, (d) 4 hollow SLA bricks, (e) 4 polyimide aerogel/SLA bricks. Also shown are states of fracture of (f) 4 hollow SLA bricks and (g) 4 polyimide aerogel/SLA bricks.

the range of 1.12–1.40 g/cm$^3$. As is intuitive, the solid acrylate (100% SLA) and solid epoxy exhibited the lowest porosity of 5.7%. An interesting observation from the data presented in Table 1 is that the inclusion of broken polyimide aerogel particles in epoxy (Polyimide aerogel/epoxy) increased the porosity to 19.3%.

The thermal properties of various monolithic materials are presented in Fig. 8. The TGA traces in Fig. 8(a) indicate higher thermal stability of polyimide (PI) than epoxy and SLA resin and higher thermal stability of post-cured SLA resin compared to epoxy. The temperature at 10% weight loss was 520 °C, 365 °C, and 375 °C respectively for PI, 100% SLA resin, and epoxy. At 650 °C, PI showed the highest char residue of 65 wt% compared to 5 wt% and 7 wt% for SLA resin and epoxy respectively. These data establish that among the material systems considered in this work, polyimide is a more suitable material for high-temperature applications. Another observation that can be gleaned from Fig. 8(a) is that the inclusion of polyimide aerogel granules in epoxy increased the char residue of the combined material but did not significantly alter the thermal degradation profile of epoxy resin. It is recalled that the PI part in the polyimide/epoxy mixed system was only 5 wt%.

The thermal conductivity values of various monolithic materials are presented in Fig. 8(b). Recall that the materials used in thermal conductivity measurements did not include the post-cured 100% SLA brick. The specimens were exposed to 50% relative humidity at room temperature for 2 months and were not dried before thermal conductivity measurement. This testing condition replicated an application environment. It is apparent that the aerogel monoliths possessed low thermal conductivity, e.g., 0.05113 W/m-K and 0.06269 W/m-K respectively for polyimide and 10 wt% SLA resin. Surprisingly, the PI aerogel/epoxy sample showed a thermal conductivity of 0.35175 W/m-K, which is counterintuitive. One would expect the porous PI aerogel particles

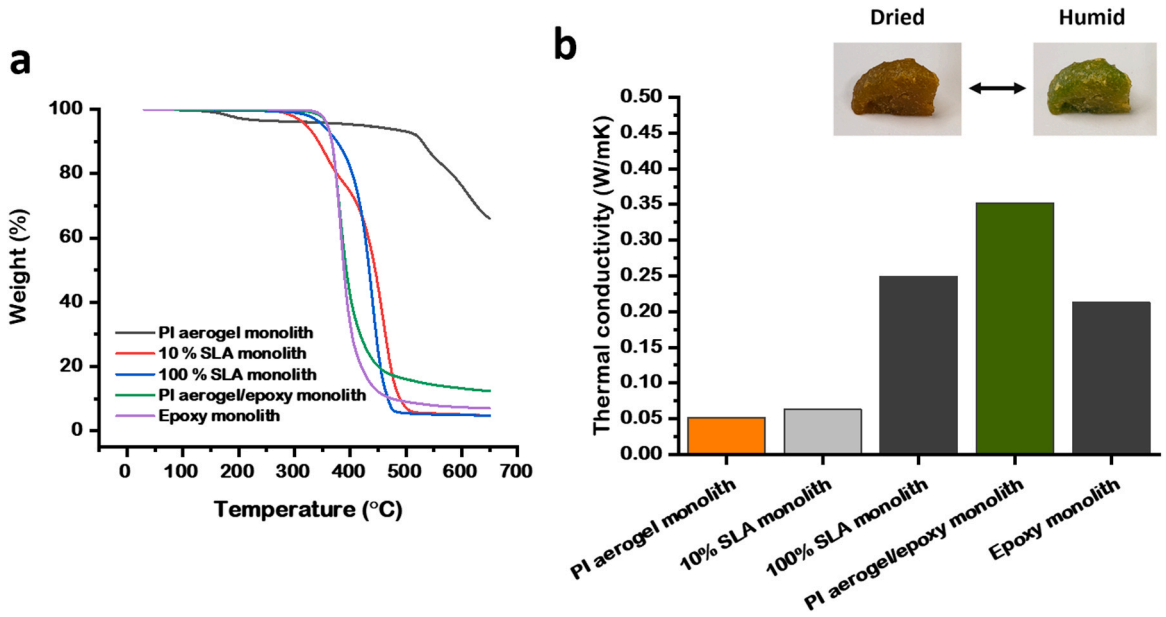


**Fig. 8.** (a) TGA traces and (b) thermal conductivity values of polyimide aerogel monolith, 10% SLA aerogel monolith, 100% SLA monolith, polyimide aerogel/epoxy monolith, and epoxy monolith. (For interpretation of the references to colour in this figure, the reader is referred to the web version of this article.)

containing air pockets to lower the thermal conductivity value compared to cured epoxy (~0.225 W/m-K). The anomalous thermal conductivity value of the epoxy/PI sample can be attributed to ingress and retention of moisture that has higher thermal conductivity (~0.6 W/m-K) [37–39]. Polyimide and epoxy backbone both are known to easily absorb moisture in an open environment [40,41]. To elucidate the effect of moisture ingress, we observed color changes of PI/epoxy sample before and after thermal treatment. The as-prepared sample was yellowish-orange, however, the specimen turned blueish orange after exposure to moisture as shown in the inset of Fig. 8(b). The original color was recovered after drying again at 80 ℃ for 24 h.

A ramification of thermal conductivity data presented in Fig. 8 was gleaned from the temperature profiles of the brick specimens subjected to heating on the heating bed of the FFF printer setup. The surface temperature of the FFF bed was set at 120 ℃ and the temperature profiles were registered using an IR camera as shown in Fig. 9. The areal temperature changes were captured as in Fig. 9(a) and plotted as a function of time. After ~570 s, the bed temperature reached the set temperature and the temperature of the specimens stabilized at 1000 s mark, as shown in Fig. 9(b). Based on Fig. 9(b), both aerogel samples - polyimide and 10% SLA resin - displayed the lowest temperature change of 18.4 and 19.9 °C respectively at 1200 s. In contrast, the other material samples, including the control SLA hollow brick, showed a temperature change of more than 23 °C at 1200 s. This is to be expected, as the meso and macroporous structure of polyimide and 10% SLA aerogels prevented heat transfer via natural convection and the trapped air pockets in these meso and macropores acted as ideal heat insulators.

We also captured the line profiles of temperature on the top surface of the samples (Fig. 9c) and registered these readings in Fig. 9(d). The lowest temperature of the control material, hollow SLA brick (Li0) was 37.5 ℃. The bricks with polyimide aerogel (Li1) and 10% SLA resin (Li2) infill showed lowest temperature of 35 ℃ and 35.5 ℃ respectively. These data support better thermal insulation properties of aerogel-filled bricks. The oscillation observed in the line profile for Li0 indicates the presence of holes in the scanning path for control material hollow SLA brick.

It is now apparent from the line scan data in Fig. 9(d) that the bricks with aerogel-infill were not uniform depth-wise or in-plane in terms of the composition of the SLA and aerogel parts. In view of this, one cannot list a unique thermal conductivity value for the SLA brick with aerogel in-fill as was discussed earlier in conjunction with only aerogels (Fig. 8b). Therefore, any efforts on thermal conductivity measurements would yield a distribution of thermal conductivity values on the measurement plane. In view of this, we resorted to thermal imaging of the brick assemblies, as shown in Fig. 10. The test specimen assembly in this case was put together randomly by picking different brick materials.

The notations 'Sp*n*, $n = 1–5$' in Fig. 10(b) and (d) indicate the spots where the temperature readings were taken. These readings helped differentiate the effects of thickness and air confined in millimeter size holes as in hollow SLA bricks and air confined in the meso- and macropores of aerogel infill. The thermal scanning was conducted in the same manner as in Fig. 9(c) and (d). The assembled bricks were placed on the FFF printer bed and the temperature of the bed was set to 120 °C. The images were taken once the actual temperature of the bed reached the set temperature. The temperature distribution reported in Fig. 10(d) was captured using a Fotric 225 IR camera. From the temperature readings at indicated spots, it is evident that PI aerogel bricks performed better than the control hollow SLA brick. The 32 mm thick surfaces at spots Sp1 and Sp4 showed 3 °C lower temperature than the spot Sp5. In addition, the surface temperature of spot Sp3 on 16 mm thick aerogel brick showed approximately 5 °C lower temperature than Sp2 on the same thickness control hollow SLA brick. The surfaces of 32 mm thick PI

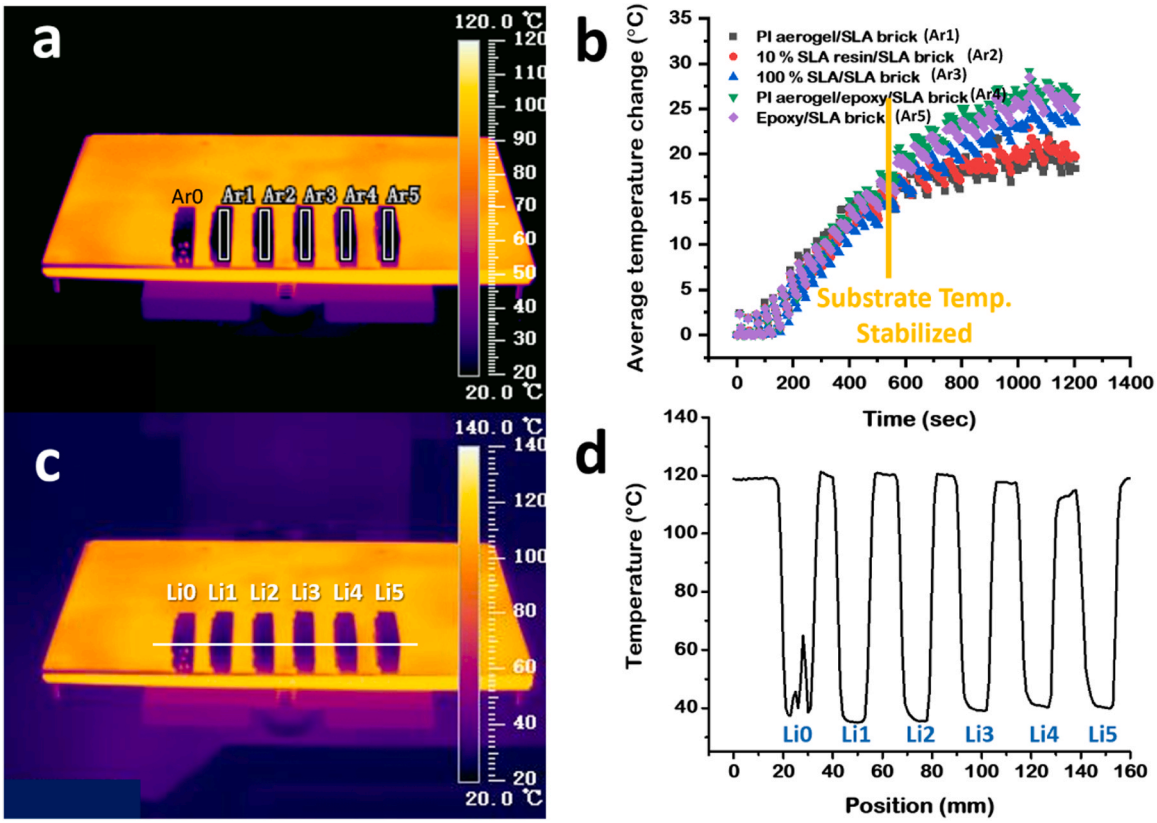


**Fig. 9.** IR camera images (a,c) and calculated areal temperature change (b) and line temperature profiles (d) of five brick specimens. The brick specimens are hollow SLA brick (Ar0, Li0), polyimide aerogel/SLA brick (Ar1, Li1), 10% SLA resin/SLA brick (Ar2, Li2), 100% SLA resin/SLA brick (Ar3, Li3), polyimide aerogel/epoxy/SLA brick (Ar4, Li4), and epoxy/SLA bricks (Ar5, Li5).

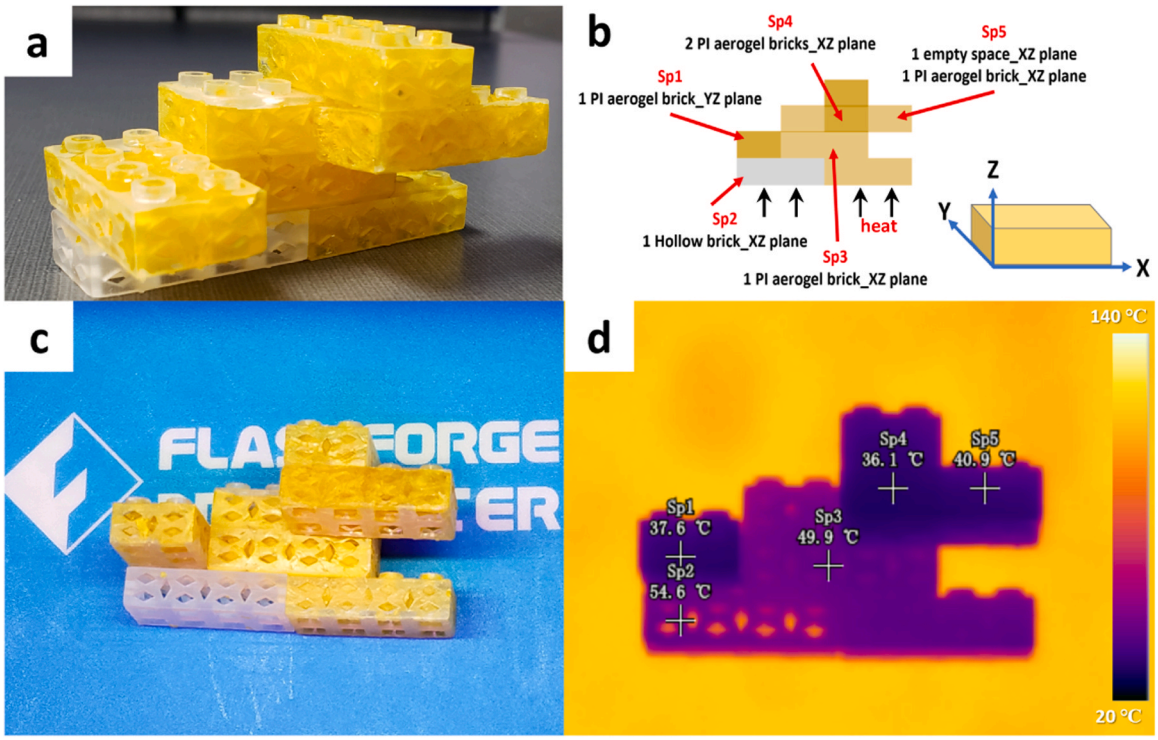


**Fig. 10.** Temperature scan data of a representative assembly of aerogel bricks. (a) Assembled brick structure with one hollow SLA brick and six PI aerogel/SLA bricks. (b) Schematic showing assembled bricks, the spots used for temperature scan reported in (d), and heat flow direction. (c) Assembled bricks placed on FFF printing bed corresponding to the arrangement in (b). (d) Spot temperature on assembled bricks in response to printing bed temperature raised to 120 °C.

aerogel bricks showed 12–14 °C lower temperature than 16 mm thick PI aerogel bricks as evident from the temperature readings at spots Sp1, Sp3, and Sp4.

## 20. Conclusion

This work demonstrates the successful fabrication of modular polyimide aerogel or acrylate aerogel bricks supported by post-cured SLA domains obtained via 3D-printing tools. These bricks can be used to build various custom structural forms for thermal insulation purposes without compromise on mechanical strength. The load-bearing post-cured acrylate bricks were fabricated from SLA resin and subsequently infused with polyimide sol or a dilute solution of SLA resin that produced corresponding gels. The data presented in this work showed that aerogel parts contributed to thermal insulation while the SLA bricks contributed to mechanical strength. The solid bricks exhibited higher thermal conductivity due to low porosity.

## CRediT authorship contribution statement

**Piljae Joo:** Conceptualization, Methodology, Investigation, Writing - original draft preparation. **Yimin Yao:** Methodology, Data curation. **Nicholas Teo:** Conceptualization, Writing - review & editing. **Sadhan C. Jana**: Conceptualization, Methodology, Writing - review & editing.

## Declaration of Competing Interest

The authors declare that they have no known competing financial interests or personal relationships that could have appeared to influence the work reported in this paper.

## Acknowledgment

This work is partially funded by National Science Foundation, United States of America under grant number CMMI 1826030.

*Supplementary Information*

Additional data on shrinkage, adhesion, and compressive stress-strain diagram.

## Appendix A. Supporting information

Supplementary data associated with this article can be found in the online version at doi:10.1016/j.addma.2021.102059.

## References

[1] S.S. Kistler, Coherent expanded aerogels and jellies, Nature 127 (1931) 741, https://doi.org/10.1038/127741a0.
[2] N. Leventis, M.M. Koebel, Aerogels Handbook. Netherlands, Springer, New York, 2011, pp. 3–18.
[3] E. Guilminot, F. Fischer, M. Chatenet, A. Rigacci, S. Berthon-Fabry, P. Achard, E. Chainet, Use of cellulose-based carbon aerogels as catalyst support for PEM fuel cell electrodes: electrochemical characterization, J. Power Sources 166 (2007) 104–111, https://doi.org/10.1016/j.jpowsour.2006.12.084.
[4] H. Rotter, M.V. Landau, M. Carrera, D. Goldfarb, M. Herskowitz, High surface area chromia aerogel efficient catalyst and catalyst support for ethylacetate combustion, Appl. Catal. B Environ. 47 (2004) 111–126, https://doi.org/10.1016/j.apcatb.2003.08.006.
[5] R. Baetens, B.P. Jelle, A. Gustavsen, Aerogel insulation for building applications: a state-of-the-art review, Energy Build. 43 (2011) 761–769, https://doi.org/10.1016/j.enbuild.2010.12.012.
[6] S.J. Kim, G. Chase, S.C. Jana, Polymer aerogels for efficient removal of airborne nanoparticles, Sep. Purif. Technol. 156 (2015) 803–808, https://doi.org/10.1016/j.seppur.2015.11.005.
[7] S.J. Kim, G. Chase, S.C. Jana, The role of mesopores in achieving high efficiency airborne nanoparticle filtration using aerogel monoliths, Sep. Purif. Technol. 166 (2016) 48–54, https://doi.org/10.1016/j.seppur.2016.04.017.
[8] S.J. Kim, P. Raut, G. Chase, S.C. Jana, Electrostatically active polymer hybrid aerogels for airborne nanoparticle filtration, ACS Appl. Mater. Interfaces 9 (2017) 6401–6410, https://doi.org/10.1021/acsami.6b14784.
[9] C. Zhai, S.C. Jana, Tuning porous networks in polyimide aerogels for airborne nanoparticle filtration, ACS Appl. Mater. Interfaces 9 (2017) 30074–30082, https://doi.org/10.1021/acsami.7b09345.

[10] C.A. García-González, M. Alnaief, I. Smirnova, Polysaccharide-based aerogels-promising biodegradable carriers for drug delivery systems, Carbohydr. Polym. 86 (2011) 1425–1438, https://doi.org/10.1016/j.carbpol.2011.06.066.
[11] S.B. Riffat, G. Qiu, A review of state-of-the-art aerogel applications in buildings, Int. J. Low -Carbon Technol. 8 (2013) 1–6, https://doi.org/10.1093/ijlct/cts001.
[12] J.P. Randall, M.A.B. Meador, S.C. Jana, Tailoring mechanical properties of aerogels for aerospace applications, ACS Appl. Mater. Interfaces 3 (2011) 613–626, https://doi.org/10.1021/am200007n.
[13] A.C. Pierre, G.M. Pajonk, Chemistry of aerogels and their applications, Chem. Rev. 102 (2002) 4243–4265, https://doi.org/10.1021/cr0101306.
[14] M.A.B. Meador, E.J. Malow, R. Silva, S. Wright, D. Quade, S.L. Vivod, H. Guo, J. Guo, M. Cakmak, Mechanically strong, flexible polyimide aerogels cross-linked with aromatic triamine, ACS Appl. Mater. Interfaces 4 (2012) 536–544, https://doi.org/10.1021/am2014635.
[15] S.J. Talley, C.L. AndersonSchoepe, C.J. Berger, K.A. Leary, S.A. Snyder, R.B. Moore, Mechanically robust and superhydrophobic aerogels of poly(ether ether ketone), Polymers 126 (2017) 437–445, https://doi.org/10.1016/j.polymer.2017.05.047.
[16] S.J. Talley, S.L. Vivod, B.A. Nguyen, M.A.B. Meador, A. Radulescu, R.B. Moore, Hierarchical morphology of poly(ether ether ketone) aerogels, ACS Appl. Mater. Interfaces 11 (2019) 31508–31519, https://doi.org/10.1021/acsami.9b09699.
[17] C. Daniel, D. Sannino, G. Guerra, Syndiotactic polystyrene aerogels: adsorption in amorphous pores and absorption in crystalline nanocavities, Chem. Mater. 20 (2008) 577–582, https://doi.org/10.1021/cm702475a.
[18] S. Malik, D. Roizard, J.M. Guenet, Multiporous material from fibrillar syndiotactic polystyrene intercalates, Macromolecules 39 (2006) 5957–5959, https://doi.org/10.1021/ma060770g.
[19] X. Wang, S.C. Jana, Tailoring of morphology and surface properties of syndiotactic polystyrene aerogels, Langmuir 29 (2013) 5589–5598, https://doi.org/10.1021/la400492m.
[20] N. Teo, S.C. Jana, Open cell aerogel foams via emulsion templating, Langmuir 33 (2017) 12729–12738, https://doi.org/10.1021/acs.langmuir.7b03139.
[21] J.K. Lee, G.L. Gould, W. Rhine, Polyurea based aerogel for a high performance thermal insulation material, J. Sol. -Gel Sci. Technol. 49 (2009) 209–220, https://doi.org/10.1007/s10971-008-1861-6.
[22] A. Shinko, S.C. Jana, M.A. Meador, Crosslinked polyurea aerogels with controlled porosity, RSC Adv. 5 (2015) 105329–105338, https://doi.org/10.1039/CSRA20788F.
[23] K. Mawhinney, S.C. Jana, Design of emulsion-templated mesoporous–macroporous polyurea gels and aerogels, ACS Appl. Polym. Mater. 1 (2019) 3115–3129, https://doi.org/10.1021/acsapm.9b00762.
[24] A. Rigacci, J.C. Marechal, M. Repoux, M. Moreno, P. Achard, Preparation of polyurethane-based aerogels and xerogels for thermal superinsulation, J. Non Cryst. Solids 350 (2004) 372–378, https://doi.org/10.1016/j.jnoncrysol.2004.06.049.
[25] N. Diascorn, S. Calas, H. Sallée, P. Achard, A. Rigacci, Polyurethane aerogels synthesis for thermal insulation - textural, thermal and mechanical properties, J. Supercrit. Fluids 106 (2015) 76–84, https://doi.org/10.1016/j.supflu.2015.05.012.
[26] S. Donthula, C. Mandal, T. Leventis, J. Schisler, A.M. Saeed, C. Sotiriou-Leventis, N. Leventis, Shape memory superelastic poly(isocyanurate-urethane) aerogels (PIR-PUR) for deployable panels and biomimetic applications, Chem. Mater. 29 (2017) 4461–4477, https://doi.org/10.1021/acs.chemmater.7b01020.
[27] N. Teo, S.C. Jana, Solvent effects on tuning pore structures in polyimide aerogels, Langmuir 34 (2018) 8581–8590, https://doi.org/10.1021/acs.langmuir.8b01513.
[28] S.L. Vivod, M.A.B. Meador, C. Pugh, M. Wilkosz, K. Calomino, L. McCorkle, Toward improved optical transparency of polyimide aerogels, ACS Appl. Mater. Interfaces 12 (2020) 8622–8633, https://doi.org/10.1021/acsami.9b17796.
[29] J. Wernery, A. Ben-Ishai, B. Binder, S. Brunner, Aerobrick - an aerogel-filled insulating brick, Energy Procedia 134 (2017) 490–498, https://doi.org/10.1016/j.egypro.2017.09.607.
[30] N. Teo, P. Joo, E.J. Amis, S.C. Jana, Development of intricate aerogel articles using fused filament fabrication, ACS Appl. Polym. Mater. 1 (2019) 1749–1756, https://doi.org/10.1021/acsapm.9b00301.
[31] S. Zhao, G. Siqueira, S. Drdova, D. Norris, C. Ubert, A. Bonnin, S. Galmarini, M. Ganobjak, Z. Pan, S. Brunner, G. Nyström, J. Wang, M.M. Koebel, W.J. Malfait, Additive manufacturing of silica aerogels, Nature 584 (2020) 387–392, https://doi.org/10.1038/s41586-020-2594-0.
[32] J. Jiang, H. Oguzlu, F. Jiang, 3D printing of lightweight, super-strong yet flexible all-cellulose structure, Chem. Eng. J. 405 (2021), 126668, https://doi.org/10.1016/j.cej.2020.126668.
[33] Q. Cheng, Y. Liu, J. Lyu, Q. Lu, X. Zhang, W. Song, 3D printing-directed auxetic Kevlar aerogel architectures with multiple functionalization options, J. Mater. Chem. A 8 (2020) 14243–14253, https://doi.org/10.1039/D0TA02590A.
[34] D.M. Smith, G.W. Scherer, J.M. Anderson, Shrinkage during drying of silica gel, J. Non Cryst. Solids 188 (1995) 191–206, https://doi.org/10.1016/0022-3093(95)00187-5.
[35] M. Papastergiou, A. Kanellou, D. Chriti, G. Raptopoulos, P. Paraskevopoulou, Poly(urethane-acrylate) aerogels via radical polymerization of dendritic urethane-acrylate monomers, Materials 11 (2018) 2249, https://doi.org/10.3390/ma11112249.
[36] S. Swyngedau, A. Nussinovitch, M. Peleg, Models for the compressibility of layered polymeric sponges, Polym. Eng. Sci. 31 (1991) 140–144, https://doi.org/10.1002/pen.760310212.
[37] K.M. Smits, T. Sakaki, A. Limsuwat, T.H. Illangasekare, Thermal conductivity of sands under varying moisture and porosity in drainage–wetting cycles, Vadose Zone J. 9 (2010) 172, https://doi.org/10.2136/vzj2009.0095.
[38] U. Berardi, R.H. Nosrati, Long-term thermal conductivity of aerogel-enhanced insulating materials under different laboratory aging conditions, Energy 147 (2018) 1188–1202, https://doi.org/10.1016/j.energy.2018.01.053.
[39] S.K. Modi, B. Durga Prasad, M. Basavaraj, Effect of moisture content and temperature on thermal conductivity of Psidium guajava L. by line heat source method (transient analysis), Int. J. Heat Mass Transf. 78 (2014) 354–359, https://doi.org/10.1016/j.ijheatmasstransfer.2014.06.076.
[40] H. Guo, M.A.B. Meador, L. McCorkle, D.J. Quade, J. Guo, B. Hamilton, M. Cakmak, Tailoring properties of cross-linked polyimide aerogels for better moisture resistance, flexibility, and strength, ACS Appl. Mater. Interfaces 4 (2012) 5422–5429, https://doi.org/10.1021/am301347a.
[41] M.R. VanLandingham, R.F. Eduljee, J.W. Gillespie, Moisture diffusion in epoxy systems, J. Appl. Polym. Sci. 71 (1999) 787–798, https://doi.org/10.1002/(SICI)1097-4628(19990131).